Inelastic strain distribution and seismic radiation from rupture of a fault kink

Benchun Duan[1] and Steven M. Day[2]

[1]   We extend an elastodynamic finite element method to incorporate off-fault plastic yielding into a dynamic earthquake rupture model. We simulate rupture for models of faults with a kink (a sharp change in fault strike), examining how off-fault plastic yielding affects rupture propagation, seismic radiation, and near-fault strain distribution. We find that high-frequency radiation from a kink can be reduced by strong plastic yielding near the kink. The reduction is significant above several Hz. When rupture propagates around the kink onto a less favorably stressed fault segment, plastic strain tends to localize into bands and lobes. Off-fault plastic yielding also significantly reduces heterogeneity of residual stresses around the kink following a dynamic event. The calculated plastic strain distribution around the kink and the radiated pulse from the kink are nearly grid independent over the range of element size for which computations are feasible. We also find that plastic strain can sometimes localize spontaneously during rupture along a planar fault, in the absence of a discrete stress concentrator like the kink. In that case, a non-dimensional parameter T, characterizing the initial proximity of off-fault material to its yield strength, determines whether plastic strain localizes into discrete bands or is smoothly distributed, with a large value of T promoting localization. However, in the cases of spontaneous localization, the details of the shear banding change with numerical element size, indicating that the final plastic strain distribution is influenced by interactions occurring at the shortest numerically resolvable scales. Off-fault plastic yielding also makes an important contribution to the cohesive zone at the advancing edge of the rupture.

1. Introduction

[2]   It has long been recognized that an abrupt change in earthquake rupture speed results in high-frequency radiation [*Madariaga*, 1977]. Observations and theoretical studies have shown that a fault kink can cause abrupt changes in rupture speed [e.g., *King and Nabelek*, 1985; *Bouchon and Streiff*, 1997; *Aochi et al.*, 2000; *Duan and Oglesby*, 2005; *Ely et al.*, 2008]. More recently, an analysis of seismic radiation from a kink on an antiplane fault performed by *Adda-Bedia and Madariaga* [2008] shows that rupture through a fault kink radiates a step function in particle velocities. A velocity step entails strong high-frequency radiation to the far field, with displacement spectrum proportional to f^{-2} (f is frequency). This analysis of the kink contribution to seismic radiation assumes, of course, that deformation in the medium surrounding the fault is purely elastic.

[3]   Detailed geological measurements on exhumed fault zones, such as the Punchbowl fault in southern California, have shown that the core of a fault, i.e., the zone with a thickness of cm to tens of cm that accommodates most of slip, is surrounded by a zone of cataclastic material with a thickness of few meters and a broader damage zone that is several hundred meter wide [e.g., *Chester and Chester*, 1998; *Ben-Zion and Sammis*, 2003; *Chester et al.*, 2004]. Trapped-wave studies [e.g., *Li et al.*, 1994; *Ben-Zion et al.*, 2003] reveal a low-velocity zone with a width of tens to hundreds of meters around the active faults in California and Turkey. A new observation of fault guided PSV-waves at SAFOD (San Andreas Fault Observatory at Depth) supports the hypothesis that the low-velocity fault zones can extend deep into the seismogenic crust [*Ellsworth and Malin*, 2006]. These observations suggest that slip during an earthquake rupture is localized on the core of a fault, and is accompanied by inelastic deformation distributed in a zone surrounding the core.

[4]   Theoretical analyses on the stress field near the tip of a steadily propagating rupture suggest that stresses elastically predicted near the rupture front can be large enough to cause failure of off-fault material, based on a Coulomb failure criterion, particularly for propagation speed near the

[1]Department of Geology and Geophysics, Texas A&M University, College Station, Texas, USA.
[2]Department of Geological Sciences, San Diego State University, San Diego, California, USA.

theoretical limiting speed for a sharp crack (e.g., the Rayleigh speed for mode II rupture) [*Poliakov et al.*, 2002; *Rice et al.*, 2005]. These studies indicate the likely importance of off-fault inelastic response for models of rupture behavior and ground motion excitation. *Andrews* [2005] has modeled this inelastic response on planar faults, using Mohr-Coulomb elastoplasticity. He has shown that, in such models, energy loss off the fault is proportional to propagation length (in 2D), and is much larger than energy loss on the fault. *Templeton and Rice* [2008] have used the similar Drucker-Prager elastoplastic model to study the extent and distribution of off-fault plasticity during seismic rupture on a planar fault. Numerical simulations by *Andrews et al.* [2007] have shown that nonlinear material response may significantly affect model predictions of near-fault ground motion.

[5] In this study, we model rupture on both planar and kinked faults, using a simple (slip-weakening) friction law, in 2D (mode II, in-plane motion). We retain the approach by *Andrews* [2005], treating off-fault material as a Mohr-Coulomb elastoplastic solid, with post-yielding behavior governed by a non-associative flow rule. Through comparisons with elastodynamic simulations for the same geometries, we examine effects of yielding on rupture propagation, strain distribution, and seismic radiation.

2. Method

[6] We modify an elastodynamic finite element method code EQdyna [*Duan and Oglesby*, 2006] to allow the off-fault material to yield when the stress state reaches a Coulomb yield criterion [*Scholz*, 2002; *Andrews*, 2005].

2.1. EQdyna: An Explicit Finite Element Method (FEM) for Elastoplastic Dynamic Analysis

[7] To perform elastoplastic dynamic analysis, the element stress cannot be calculated from displacement, as it can in elastodynamic analysis. Rather, the element stress must be updated from the previous time step value by integrating the stress rate. The stress rate can be computed from the element nodal velocity. The general structure of EQdyna [*Duan and Oglesby*, 2006] does not require change. The major modifications involve only the element stress calculation and implementation of the stiffness-proportional Rayleigh damping at the element level.

[8] From the element point of view, the internal force for elastic analysis can be computed by [e.g., *Hughes*, 2000]

$$f^e = k^e d^e = 4jB^T DBd^e, \tag{1}$$

where f^e, d^e, k^e are the nodal force vector, the displacement vector, and the element stiffness matrix, respectively, j is the Jacobin determinant, and B and D are, respectively, the strain-displacement matrix and the constitutive matrix with standard definition in the FEM literature [e.g., *Hughes*, 2000]. Equation (1) is based upon one-point Gaussian Quadrature, which (in 2D) accounts for the pre-factor of 4 appearing in (1). In the code, one does not have to calculate the element stiffness matrix. Rather, the multiplication on the right hand of equation (1) can be performed from right

to left. In this point of view, the element strain and stress vectors at the integration point are

$$\varepsilon^e = Bd^e, \\ \sigma^e = D\varepsilon^e, \tag{2}$$

where, the superscript e denotes "element", indicating the element point of view of the quantities. In elastic analysis, one does not need to explicitly calculate the element strain and stress if they are not required for analysis. However, the element stress is required in elastoplastic analysis to assess the Coulomb yield criterion. We remark that the element stress is calculated at the Gaussian quadrature point (the center of the element), while the internal force is evaluated at the element nodes.

[9] For elastoplastic dynamic analyses, we require the elastic stress increments (which may be subsequently modified by the yield condition) at each time step. One can evaluate them from element strain rate and stress rate at the integration point, using the time derivatives of (2),

$$\dot{\varepsilon}^e = Bv^e, \\ \dot{\sigma}^e = D\dot{\varepsilon}^e, \tag{3}$$

where overdot represents the time derivative, and v^e is the velocity vector. Then the element stress at the time step $n + 1$ can be updated from the value of the previous time step n through time integration, approximated by

$$\sigma_{n+1}^e = \sigma_n^e + \dot{\sigma}^e \Delta t, \tag{4}$$

where Δt is the dynamic simulation time step. This is the trial element stress and may be altered if plastic yielding occurs. In this update scheme, velocity, strain rate, and stress rate are evaluated at the time $(n + 1/2) \Delta t$. Then the internal nodal force vector (at the element level) at the time step n + 1 can be calculated as

$$f_{n+1}^e = 4jB^T\sigma_{n+1}^e. \tag{5}$$

[10] In addition to the above modification in the internal force calculation, the implementation of the stiffness-proportional Rayleigh damping [e.g., *Hughes*, 2000] also needs to be revised. In elastic analyses, one can easily implement the damping by adding a correction vector qv^e to the displacement vector d^e before calculating the internal force [*Hughes*, 2000; *Duan and Oglesby*, 2006]. Here, q is the damping coefficient. In elastoplastic analyses, this damping force needs to be calculated separately from the internal force. Using the above notation, one can calculate the element damping force vector at the time step n + 1 from the stress rate at the time $(n + 1/2) \Delta t$ as

$$f_{n+1}^{damp} = 4jqB^T\dot{\sigma}^e. \tag{6}$$

[11] In the new version of the code EQdyna, we still use the traction-at-split-node (TSN) treatment for the fault boundary [*Andrews*, 1999]. In this method, a given fault plane node is split into two halves, which interact through traction acting on the interface between them. The calculated
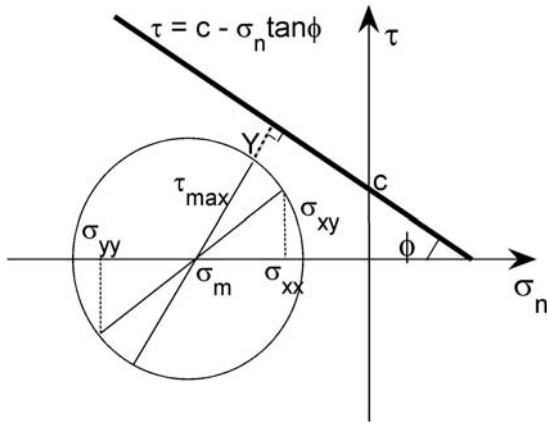
Figure 1. Mohr-Coulomb yield criterion. Y is a point on the circle.

fault-plane nodal tractions (shear and normal components) represent averages over adjacent element edges, that is, each is a nodal force divided by an effective element-edge area; the fault boundary conditions are enforced for these averaged quantities. We adopt the formulation given by *Day et al.* [2005] in the new version, which provides a consistent treatment for fault behavior (at a given pair of split nodes) at all times, including pre-rupture, rupture initiation, arrest of sliding, and possible reactivation and arrest of sliding. In this work, rupture is artificially initiated from the uniform stress state by prescribing stress drops on the fault behind a rupture front that propagates at a fixed speed (2000 m/s, which is two thirds of the shear wave speed in the models of this study). This artificial initiation is enforced within a nucleation zone with half length of L_0. Beyond this zone, rupture propagates spontaneously. This initiation scheme is similar to that used by *Andrews* [2005] for similar calculations with nonelastic off-fault response.

2.2. Off-Fault Elastoplastic Material Behavior

[12] We incorporate off-fault plastic yielding as an approximate continuum representation of the brittle damage mechanisms that dominate nonlinear deformation in the upper crust. The Mohr-Coulomb yield criterion that we use is pressure-sensitive, postulating that yield in a body occurs on a plane when the normal (σ_n, positive in tension in this study) and shear (τ) stresses reach a critical combination. The criterion requires that the pair (σ_n, τ) resolved onto any plane satisfy

$$|\tau| - (c - \sigma_n \tan \phi) \leq 0, \qquad (7)$$

where c is cohesion and ϕ is the internal friction angle. In 2D plane strain calculations, we assume that the maximum and minimum principal stress directions are in the x-y plane. To simplify calculations, one can express the yield criterion in terms of the maximum shear stress over all orientations at a point, $\tau_{\max}$, and the mean stress, σ_m, both of which can be calculated from relevant stress components $\sigma_{xy}, \sigma_{xx}, \sigma_{yy}$. As shown by the Mohr circle construction in Figure 1, for given $\tau_{\max}$ and σ_m, the left-hand side of (7) is maximum at stress state Y, at which (σ_n, τ) are given by

$$(\sigma_m + \tau_{\max} \sin \phi, \tau_{\max} \cos \phi), \qquad (8a)$$

where,

$$\tau_{\max} = \sqrt{\sigma_{xy}^2 + \left[(\sigma_{xx} - \sigma_{yy})/2\right]^2}, \qquad (8b)$$

and

$$\sigma_m = \frac{1}{2}\left(\sigma_{xx} + \sigma_{yy}\right). \qquad (8c)$$

[13] Substituting (8) into (7), one obtains an alternative expression for the yield condition,

$$\tau_{\max} - (c \cos \phi - \sigma_m \sin \phi) \leq 0. \qquad (9)$$

and we can write (9) as

$$\tau_{\max} \leq \tau_{Coulomb} \qquad (10)$$

where we define

$$\tau_{Coulomb} = c \cos \phi - \sigma_m \sin \phi. \qquad (11)$$

[14] The plastic flow rule in this work is similar to that used by *Andrews* [2005]. If the criterion (10) is violated, stresses are adjusted to the yield line with two constraints: (1) there is no change in mean compressive stress σ_m; (2) the shear stress components σ_{xy} and $(\sigma_{xx} - \sigma_{yy})/2$ are reduced by a common factor. The increment of the plastic strain tensor $\delta \varepsilon_{ij}^p$ can be calculated from the adjustment to each stress component $\delta \sigma_{ij}$ and shear modulus G by $\delta \varepsilon_{ij}^p = \delta \sigma_{ij}/G$. The magnitude of plastic strain (permitting no plastic dilation) at a time can be calculated by

$$\varepsilon^p = \sqrt{\left[(\varepsilon_{xx}^p - \varepsilon_{yy}^p)/2\right]^2 + (\varepsilon_{xy}^p)^2}. \qquad (12)$$

[15] In implementation, we first use the stress components estimated from equation (4), that is, using elastic stress increments, to assess whether the criterion (10) is violated at the current time step. If it is not violated, the stress from equation (4) is directly used to calculate the internal force. If it is violated, we perform the adjustment in the stress deviator domain, similar to that used by *Andrews* [2005]. Applying the factor of $\tau_{coulomb}/\tau_{\max}$ to each stress deviator component will adjust the stress state exactly onto the yield line at the current time step $n + 1$. Then the stress components after adjustment are recovered from the mean stress and the adjusted stress deviators, and the plastic strain increments are calculated. In this case, the adjusted element stress, rather than that in equation (4), is used to calculate the internal force. As usual in models of materials in which the configuration of the yield surface (i.e., the function of the stress components that defines the elastic limit) is pressure-dependent, this flow rule is non-associative, that is, plastic strain increments are not orthogonal to the yield surface (non-associated flow rules are often appropriate for materials such as rocks [e.g., *Davis and Selvadurai*, 2002]), and non-dilatant.

2.3. Two Numerical Regularization Schemes

[16] The elastoplastic analysis is nonlinear. Since high-frequency components of the solution do not simply superimpose linearly on low-frequency components, the inevitable numerical inaccuracies at wavelengths near the resolution limit of the mesh, if not controlled, can potentially contaminate the solution over all space-time scales. Therefore some

Table 1. *Andrews* [2005]'s Model Parameters

σ_{xx}^{0}	σ_{yy}^{0}	σ_{xy}^{0}	tan ϕ	c	ρ	Vp	Vs	μ_s	μ_d	T_v
−50 MPa	−50 MPa	10 MPa	0.75	0 MPa	2700 kg/m^3	5196 m/s	3000 m/s	0.5	0.0	0.0067 s

form of numerical regularization is usually necessary to suppress solution components with spatial scale near that resolution limit. We apply two schemes to regularize calculations in the code: one is stiffness-proportional Rayleigh damping; the other is Maxwellian viscoplasticity (time-dependent relaxation of the stress adjustment). The former introduces a Q (seismic quality factor, which characterizes the rate of decay of seismic waves) that is inversely proportional to frequency, and therefore selectively damps wavelengths (λ) near the resolution limit of the numerical mesh. The damping parameter q can be specified through a non-dimensional parameter β, such that q = $\beta\Delta$t, or equivalently,

$$q = \beta\alpha\Delta x/v_p. \qquad (13)$$

where Δx is the minimum element dimension, α is the Courant-Friedrich-Lewy (CFL) number and Vp is the P wave velocity. Then holding β fixed while the mesh is refined (at fixed CFL number) has the effect of shifting the absorption band such that Q is unchanged as a function of $\lambda/\Delta x$. Alternatively, one can hold q itself fixed to keep the absorption band invariant as a function of λ.

[17] The second scheme, viscoplasticity, was used by *Andrews* [2005] to regularize elastoplastic rupture simulations. In this scheme, the abrupt relaxation of the trial stress (4) is replaced by a smoothed relaxation with some exponential decay time T_v. That is, the stress adjustment factor $\tau_{coulomb}/\tau_{max}$ is replaced by $\{1 - (1 - \tau_{coulomb}/\tau_{max})[1 - \exp(-\Delta t/T_v)]\}$. We remark that a smaller T_v results in faster relaxation of the trial stress to the yield surface and thus causes stronger off-fault plastic yielding that in turn leads to slower rupture propagation.

[18] Both numerical parameters β and T_v have the intended effect of removing poorly-resolved short-wave-length features from the solution, and ideally we would like the solution to be relatively insensitive to their precise values. Values of β of order 0.1 have been found effective in reducing short-wavelength noise in elastodyanamic rupture simulations [*Day et al.*, 2005; *Duan and Oglesby*, 2006, 2007; *Dalguer and Day*, 2007]. Values of T_v of order $\Delta x/V_s$ (with V_s the S wave speed) were successfully used by *Andrews* [2005] to reduce short-wavelength noise in elasto-plastic rupture simulations.

2.4. Code Verification: Revisiting the Model by Andrews

[19] To verify our numerical implementation, we run a simulation for the same 2D (inplane) model studied by *Andrews* [2005]. As in that study, the initial stress field is uniform, friction on a planar fault is governed by a time-weakening law with a critical time of $Tc = 0.0035$ s, and the simulation uses viscoplasticity regularization, with a value of $Tv = 0.00067$ s. Model parameters are summarized in Table 1, and we refer to *Andrews* [2005] for specifics of the time-weakening law, which we use only for this verification test.

[20] Figure 2 shows time histories of stresses at $x = 1$ km and $x = 2$ km from the initiation point, and Figure 3 shows slip velocity time histories at those points. For comparison, these Figures 2 and 3 also show the corresponding results from *Andrews* [2005]. The amplitude, timing, and duration of these time histories match those of Andrews with good precision (timing differences less than 0.2%, peak amplitude differences less than 7%). The spatial distribution of the late-time (0.785 s) plastic strain magnitude (equation (12)) is also nearly identical between the two solutions, as shown in Figure 4. We also note that viscoplastic regularization proved unnecessary for obtaining a stable solution in this
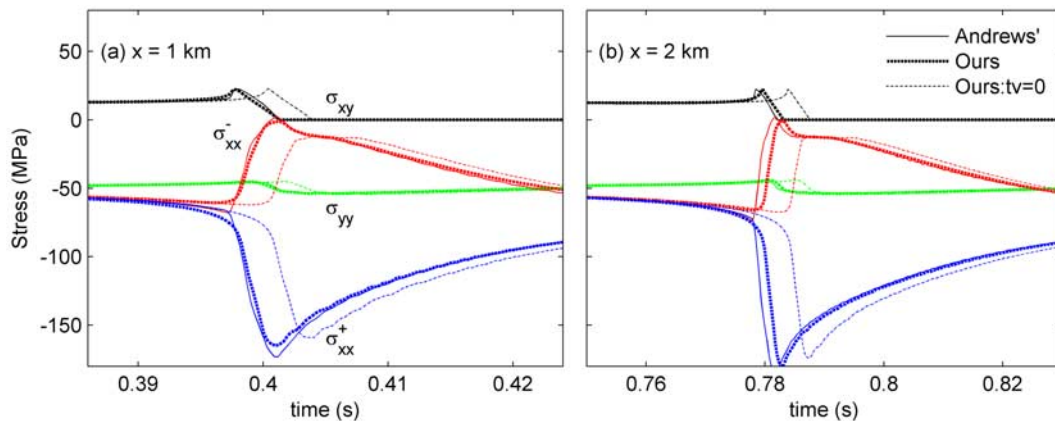

Figure 2. Comparison of time histories of stresses at (left) $x = 1$ km and (right) $x = 2$ km on the model by *Andrews* [2005]. σ_{xy} and σ_{yy} are continuous across the fault, while σ_{xx} in adjacent elements of the fault shows extensional on one side ($y < 0$, σ_{xx}^{-}) of the fault and compressive on the other side ($y > 0$, σ_{xx}^{+}). Time differences are less than 0.2%, and peak amplitude differences are less than 7% between our results and those of *Andrews* [2005].
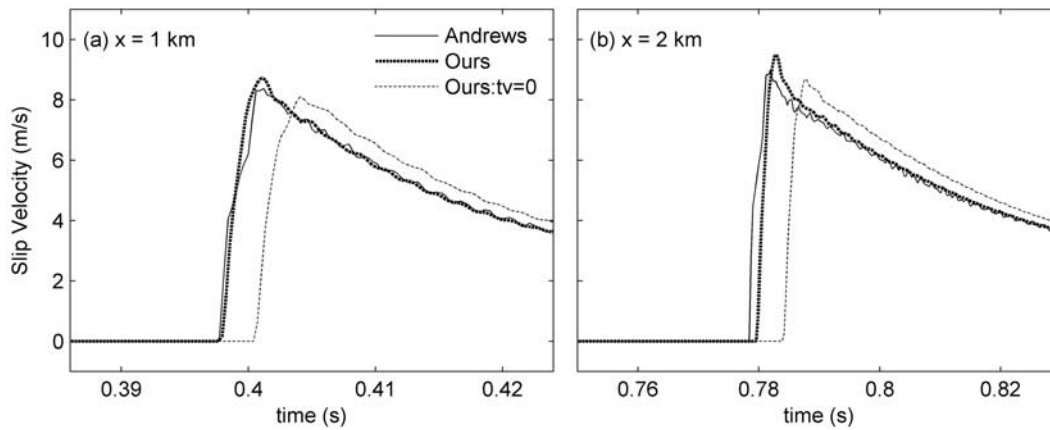
Figure 3. Comparison of time histories of slip velocity at (left) $x = 1$ km and (right) $x = 2$ km on the model by *Andrews* [2005]. Time differences are less than 0.2%, and peak amplitude differences are less than 7% between our results and those of *Andrews* [2005].

particular problem by our method. This is clear from the comparison of the above results with those from a simulation with $Tv = 0$ s, also shown in Figures 2–4. For this model, then, Tv in the 0–0.00067 s range has a very small effect on rupture velocity (Tv of 0.00067 producing about a 0.7% advance of rupture time relative to the inviscid case) and no visible effect on plastic strain distribution. The result from the above model of Tv having little effect on rupture velocity and plastic strain distribution is not a general finding, however, as we discuss later.

3. Dynamics of Faults With a Kink With Off-Fault Plastic Yielding

[21] We examine the effects of off-fault yielding on the rupture features and seismic radiation associated with a fault

kink. Our model is a simple 2D strike-slip fault with a change in strike. We first explore one such kinked fault model in detail and then examine several variations of the model.

3.1. Results for a Kink Model

3.1.1. Model

[22] Figure 5 shows a 2D right-lateral strike-slip fault consisting of two straight segments. The left segment occupies the x axis, and there is a change of 10° in the strike at the intersection point with the right segment, which is at the coordinates $x = 10$ km and $y = 0$ km. For this type of sharp kink, there is a singularity in stress at the kink in analytical solutions [e.g., *Tada and Yamashita*, 1997]. In our numerical treatment, as done in the study by *Duan and Oglesby* [2005], we define a kink element at the intersection.
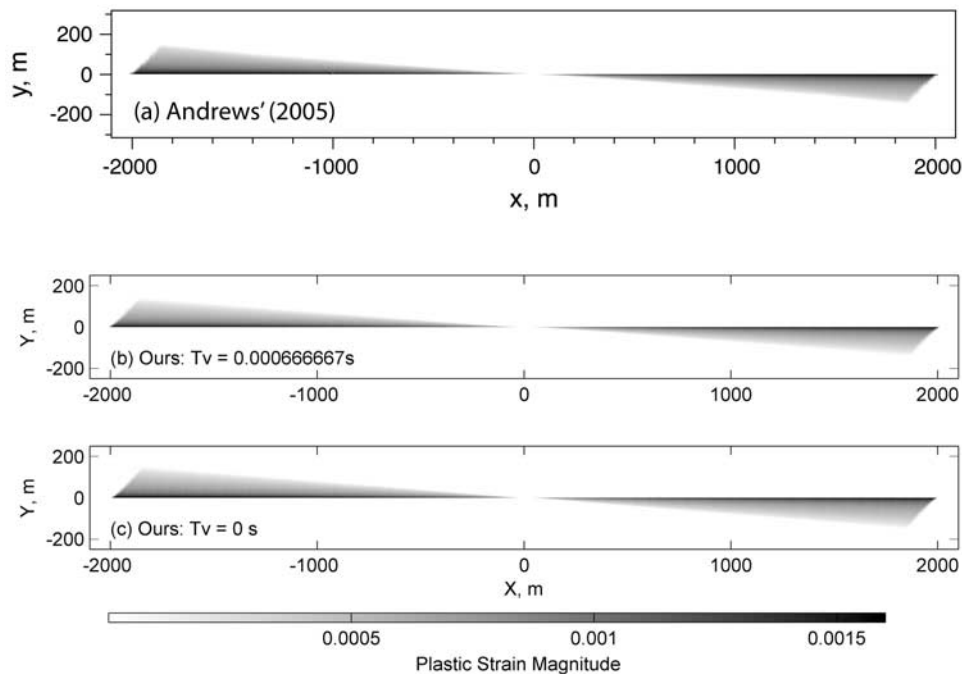

Figure 4. Comparison of magnitude of plastic strain at time 0.785 s on the model by *Andrews* [2005].
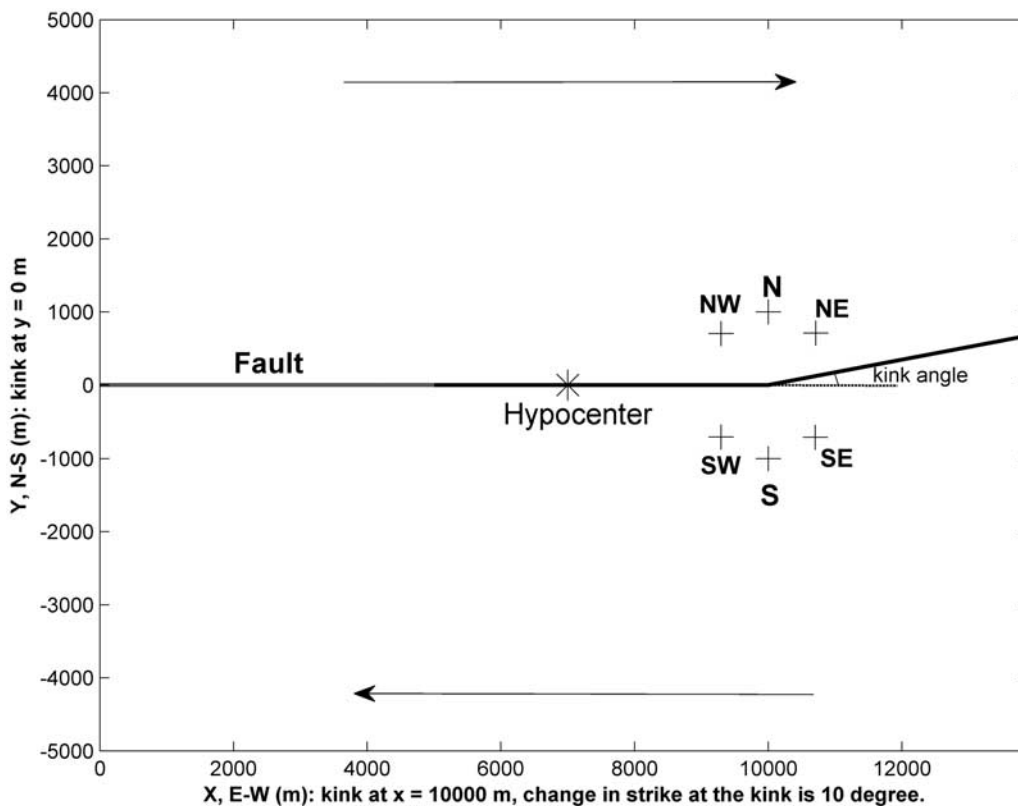
Figure 5. Geometry of a 2D right-lateral strike-slip fault with a kink. Six concentric stations 1 km away from the kink are labeled by their orientations relative to the kink.

The left end of the element belongs to the left segment of the fault, and the right end of the element belongs to the right segment of the fault, in terms of their fault normal and shear directions. By this treatment, the singularity at the kink is smeared out over the kink element. We consider a uniform pre-stress field, with $\sigma_{xx} = \sigma_{yy}$, so that the left segment occupies a plane of maximum shear stress σ_{xy} and the right segment of the fault is therefore less favorable for rupture propagation compared with the left segment. The rupture starts at $x = 7$ km, within a nucleation patch with a half-length of 330 m. We use the linear slip-weakening friction law in which the static coefficient of friction μ_s drops linearly to the dynamic coefficient μ_d over a critical slip distance D_0. Material properties, frictional parameters, pre-stress values, and numerical regularization parameters of the model are listed in Table 2.

[23] We examine velocity time histories at stations located at six azimuths with respect to the kink, on each of 7 concentric circles at radial distances r of, respectively, 0.1, 0.2, 0.3, 0.5, 1, 1.5, and 2 km. The six stations with r = 1 km are shown in Figure 5. The calculations use quadrilateral elements along and near the fault, and we denote this near-fault element length by Δx. The element size then increases gradually away from the fault (to improve the computational

efficiency), and the boundaries of the model are far enough away to prevent boundary reflections from contaminating the space-time region that we will examine.

[24] To provide a reference model to aid in the identification of plastic yielding effects, we also perform a rupture simulation for the same model, but with linearly elastic off-fault response. The only change in the latter calculation relative to the former (elastoplastic) case is setting the cohesion c in Table 2 to be a very high value (e.g., 10^{30} MPa) to suppress plastic yielding in the model. As an aid to isolating the pulse radiated from the kink in these two models, we also run elastoplastic and elastic simulations on a planar fault model, in which the fault is along y = 0 km, without a change in strike. Most simulations are performed with $\Delta x = 5$ m, with the damping parameter β as shown in Table 2. We also run several simulations with $\Delta x = 2.5$ m to examine convergence of the solution. In those cases, we hold damping q fixed (requiring an increase to 0.2 of the dimensionless parameter β).

3.1.2. Rupture Dynamics of the Fault With a Kink

[25] Figure 6 shows rupture time versus distance along the fault strike from the above four simulations. Rupture time is defined as the moment at which the shear stress reaches the yield stress level at a point on the fault. In the

Table 2. Material and Computational Parameters for the Elastoplastic Calculation in Section 3.1

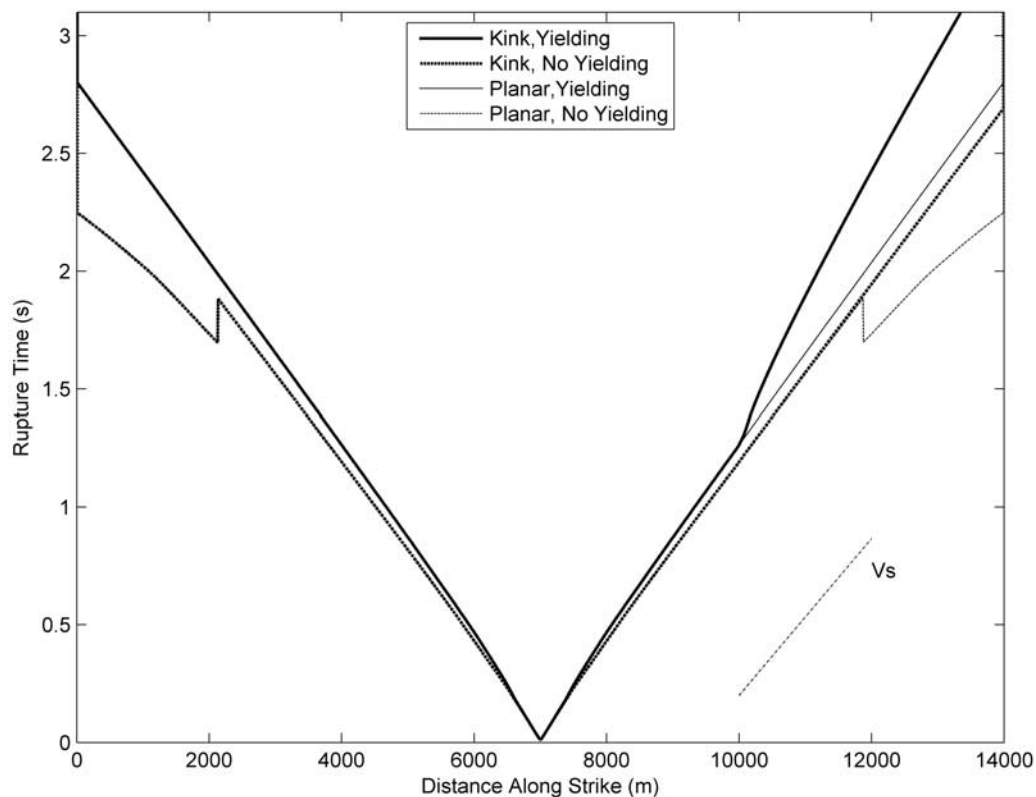| $\sigma_{xx}{}^0$	$\sigma_{yy}{}^0$	$\sigma_{xy}{}^0$	$\tan\phi$	c	D_0	ρ	Vp	Vs	μ_s	μ_d	T_v	α	β
−100 MPa	−100 MPa	45 MPa	0.75	0 MPa	0.15 m	2700 kg/m³	5196 m/s	3000 m/s	0.6	0.3	0.0017 s	0.3	0.1

Figure 6. Rupture times along a kinked fault and a planar fault with off-fault elastic and elastoplastic responses. Off-fault plastic yielding significantly decelerates rupture propagation at the fault kink.

reference simulation–straight-fault, elastodynamic off-fault behavior (light dashed curve)–rupture rapidly accelerates to within 1% of the Rayleigh velocity, then undergoes a supershear transition (by the daughter-crack mechanism of *Andrews* [1976]) at a propagation distance of just under 5 km.

[26] We examine the effects of introducing yielding and a fault bend to the reference case, first separately and then together.

[27] 1. When yielding is permitted in the straight-fault model (light solid curve), its effect on rupture propagation is modest: rupture acceleration is reduced slightly (less than 4% relative to the subshear portion of the elastodynamic case), and the supershear transition is suppressed (at least over the 7 km of propagation distance computed here).

[28] 2. When a fault kink, with a change of 10° in strike, is added in the elastodynamic case, it causes no perceptible change in rupture speed relative to the unkinked elastodynamic case (i.e., there is no obvious change in slope of the heavy dashed curve at the kink), but it does suppress the supershear transition (within the available 7 km rupture length).

[29] 3. Finally, when both the 10° kink and off-fault yielding are introduced (heavy solid curve), the rupture speed is significantly reduced upon passage through the fault kink. Furthermore, while there is some subsequent acceleration of rupture, its velocity stays at a low level throughout the entire right segment. The reduction in the rupture speed at the fault kink and the slow rupture speed on the right segment are associated with significant off-fault plastic deformation near the kink and along the right

segment, as illustrated by the plastic strain magnitude in Figure 7a. *Andrews* [2005] proposed that the off-fault plastic work be viewed as effectively adding an additional component to the fracture energy, over and above the work of slip weakening. That viewpoint is consistent with our finding of reduced rupture velocities in the cases with plastic yielding.

3.1.3. Distribution of Off-Fault Plastic Strain

[30] The plastic strain distribution shown in Figure 7a indicates that there is significant strain localization associated with the fault kink, principally on the side of the fault that is associated with extension in the ε_{xx} component of strain at the advancing rupture front (i.e., the lower, or $-y$, side in Figure 7a). One long, narrow band of high plastic strain originates from the kink and extends more than 2 km in the SEE direction, making an angle of about 17° with respect to the x axis. Development of this plastic strain band in our continuum model is suggestive of the development or mobilization of one or more secondary faults during the dynamic event, helping to accommodate flow around the sharp (10°) change in the strike of the main fault. Other localized plastic strain features includes (1) a strong, large strain lobe extending below the kink; (2) a strong but small strain lobe occurring to the left of the kink; (3) a weak, small strain lobe extending above the kink; and (4) a short-strain band occurring to the right of the kink.

[31] Localized features like the above pose considerable computational challenge. The spatial scale of the strain concentrations may ultimately be limited only by the grid spacing, rendering the solution inherently mesh-dependent.
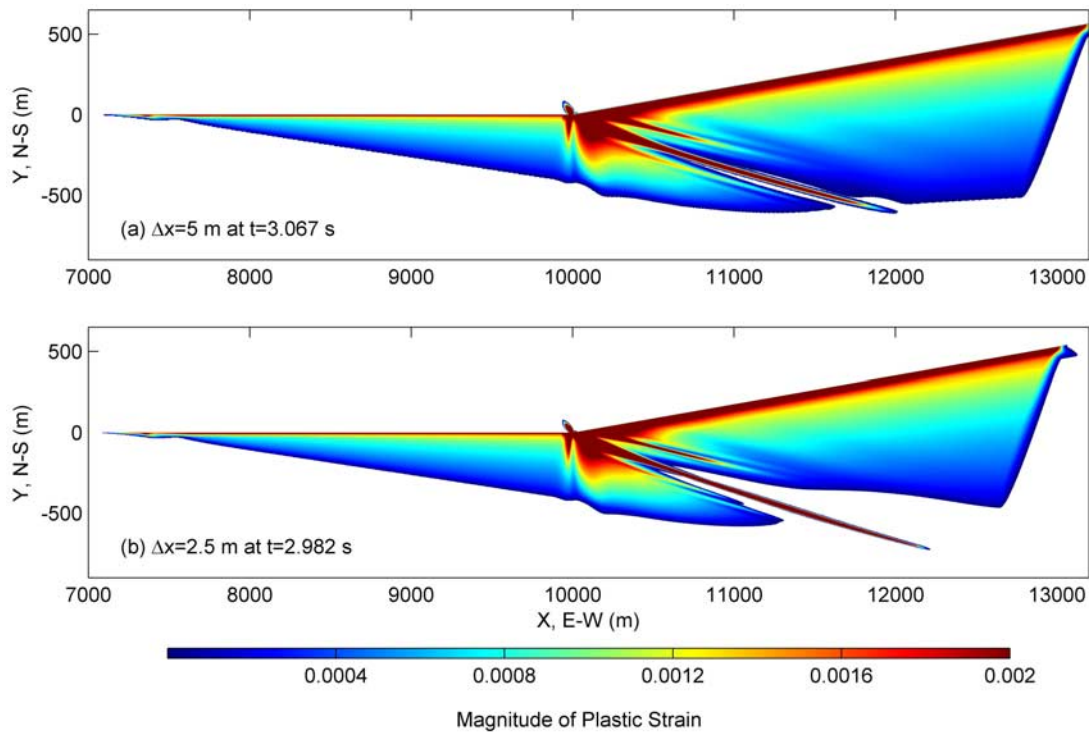
Figure 7. Distribution of off-fault plastic strain magnitude due to rupture on a fault with a kink. Plastic strain localizes into bands and lobes near the kink, and the solution of the localization is apparently convergent when the element size is reduced.

We see some evidence of this effect when we compare solutions done with different grid spacings Δx, despite the measures taken to regularize the problem. Figure 7b shows the plastic strain distribution for kinked-fault problem with Δx reduced by a factor of 2 (2.5 m, versus 5 m for the case shown in Figure 7a). The long, strong shear band becomes sharper and the area without plastic strain surrounding it becomes larger when the numerical element size is reduced. On the other hand, the number, location and general shape of the plastic strain bands and lobes do not change. Furthermore, we show later that the radiated wavefields are essentially indistinguishable between the 5 m and 2.5 m cases. In the practical sense, then, the solution appears to be essentially grid-size independent, despite the plastic strain localization associated with the fault kink.

[32] The change in fault strike also affects the smooth part of the plastic strain field to the right of the kink. Plastic deformation along the right segment of the fault is much more intense, and the width of plastic strain zone is much wider, than that along the left segment. This behavior corresponds to intensified inelastic deformation when rupture propagates onto the fault segment that is less favorably oriented for rupture in the given pre-stress field.

3.1.4. Reduction of High-Frequency Radiation From the Kink

[33] The inelastic strain localization associated with a fault kink discussed above has significant effects on seismic radiation from the kink. Elastic analysis [*Adda-Bedia and Madariaga*, 2008] has shown that seismic radiation from a kink on an antiplane (Mode III) fault has first motion that is a step function in particle velocity, which implies a contribution to the high-frequency displacement-amplitude spectrum that is proportional, asymptotically, to f^{-2}. Figure 8 shows x-component particle velocity waveforms at Station S (see Figure 5) from six simulations. The cases simulated include the kinked fault model with two element sizes (to establish grid independence), and the planar fault model for reference. For each of these three models, two calculations are performed, with elastic and elastoplastic off-fault responses, respectively. In each kinked-fault case, we can examine departure of the wavefield time history from the corresponding planar fault curve to identify the radiated pulse from the kink. Using failure time of the kink (i.e., rupture arrival time at $x = 10$ km, from Figure 6), velocity of the medium (Table 2), and the distance r = 1 km, we identify the abrupt velocity jump that is present just beyond 1.5 s in the elastodynamic kinked-fault model (but absent in the straight-fault model) as the S-wave radiation originating from the kink. This velocity jump in the elastodynamic solution is as near to an instantaneous step as we can resolve numerically, and is therefore consistent with theoretical expectations from the analysis of *Adda-Bedia and Madariaga* [2008] (i.e., presuming the Mode III asymptotic behavior to hold for Mode II as well). Comparison of waveforms from the two element sizes confirms that the elastodynamic rupture problem is grid independent to high precision, the only visible difference being that the $\Delta x = 2.5$ m solution eliminates the small, high-frequency overshoot in the $\Delta x = 5$ m solution at the time of the kink-related velocity step.

[34] The elastoplastic solutions initially follow the elastodynamic solutions fairly closely, apart from accumulating a small delay amounting to about 0.1 s by the time of the kink S-wave arrival, as would be expected from rupture
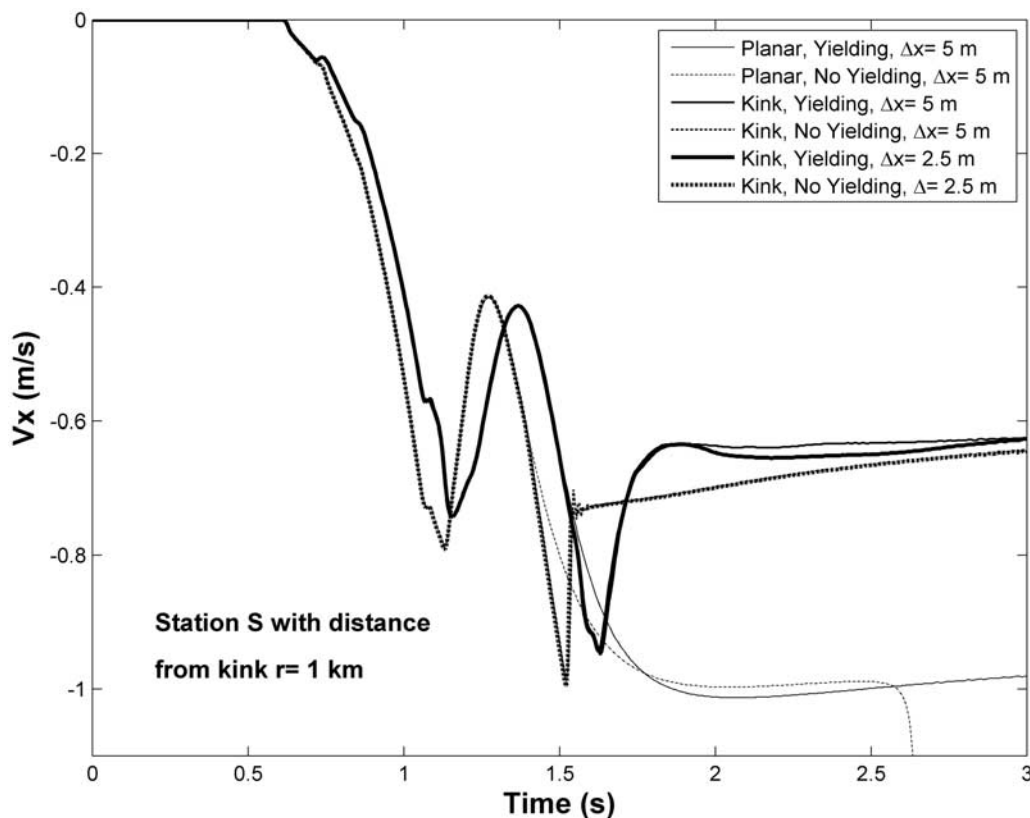
Figure 8. Particle velocity time histories at Station S from six simulations: a kinked fault model with two element sizes and a planar fault model. Two calculations with off-fault elastic (no yielding) and elastoplastic (yielding) responses are performed on each model. Velocity jumps beyond 1.5 s from the kinked fault model are caused by seismic radiation from the kink.

velocity difference shown in Figure 6. The kink S-wave arrival itself is significantly different in the elastoplastic case, however. In contrast to the essentially instantaneous step seen in the elastodynamic case, the kink arrival in the elastoplastic case is smoothed significantly, with a ramp-like first motion followed by a roughly exponential decay of slope. Since wavefield singularities propagate to the far field, this change in the order of singularity signals an increased decay rate in the far-field spectral asymptote from f^{-2} to f^{-3}, as regards the contribution of the kink to the radiated displacement spectrum. Roughly speaking, the spectral transition will be centered at frequency of the order of the initial-ramp slope divided by the step amplitude, i.e., the inverse rise time. For the purpose of estimating somewhat more quantitatively the high-frequency reduction associated with this smoothing of the kink S-wave, we note that, as shown in Figure 9a, the simple function $[1 - \exp(-t/T)]H(t)$, with t measured from the arrival time of the kink S wave, fits the initial part of the velocity jump quite well, with $T = 0.062$ s. The spectrum of this function is $1/(2\pi f \sqrt{1 + (2\pi f)^2 T^2})$, where f is frequency in Hz. The spectrum of this function initially follows the f^{-1} slope of the step function, but (with this value of T) shows a transition in slope to f^{-2}, with corner at about 2.7 Hz (Figure 9b). Seismic radiation from the kink above this frequency is significantly reduced by off-fault plastic yielding, compared with the case in which off-fault response is

elastic. Note that the initial part of the S-wave pulse from the kink also appears to be grid independent, as judged from the agreement between $\Delta x = 2.5$ m and 5 m elastoplastic solutions in Figure 8. Some difference between elastoplastic solutions for the two element sizes becomes visible after about 2 s (heavy and intermediate solid curves), and this may be a manifestation of the small grid-dependent differences in plastic strain localization discussed above.

[35] Effects of off-fault plastic yielding on seismic radiation from a fault kink vary spatially. Figure 10 shows x-component particle velocities at six stations (see Figure 5) that are 1 km away from the fault kink in six directions. Station S has been examined in detail above. As shown in Figure 10, seismic radiation from the kink arrives these stations at around 1.5 s. The reduction of high-frequency radiation from the kink due to off-fault plastic yielding can also be clearly observed at stations SW and NW, indicated by more gentle slopes of the velocity jumps in the elasto-plastic calculation than those in the elastic calculation. Two velocity jumps around 1.5 s at each of the two stations correspond to P and S wave pulses, respectively, from the kink. The second velocity jump (S wave pulse) at Station NW has opposite polarities between the elastic and elasto-plastic calculations. No obvious reduction is observed at Station N. The radiation from the fault kink is not well separated from other phases at Stations NE and SE. The waveforms of these two stations from the elastoplastic calculation are significantly different from those from the
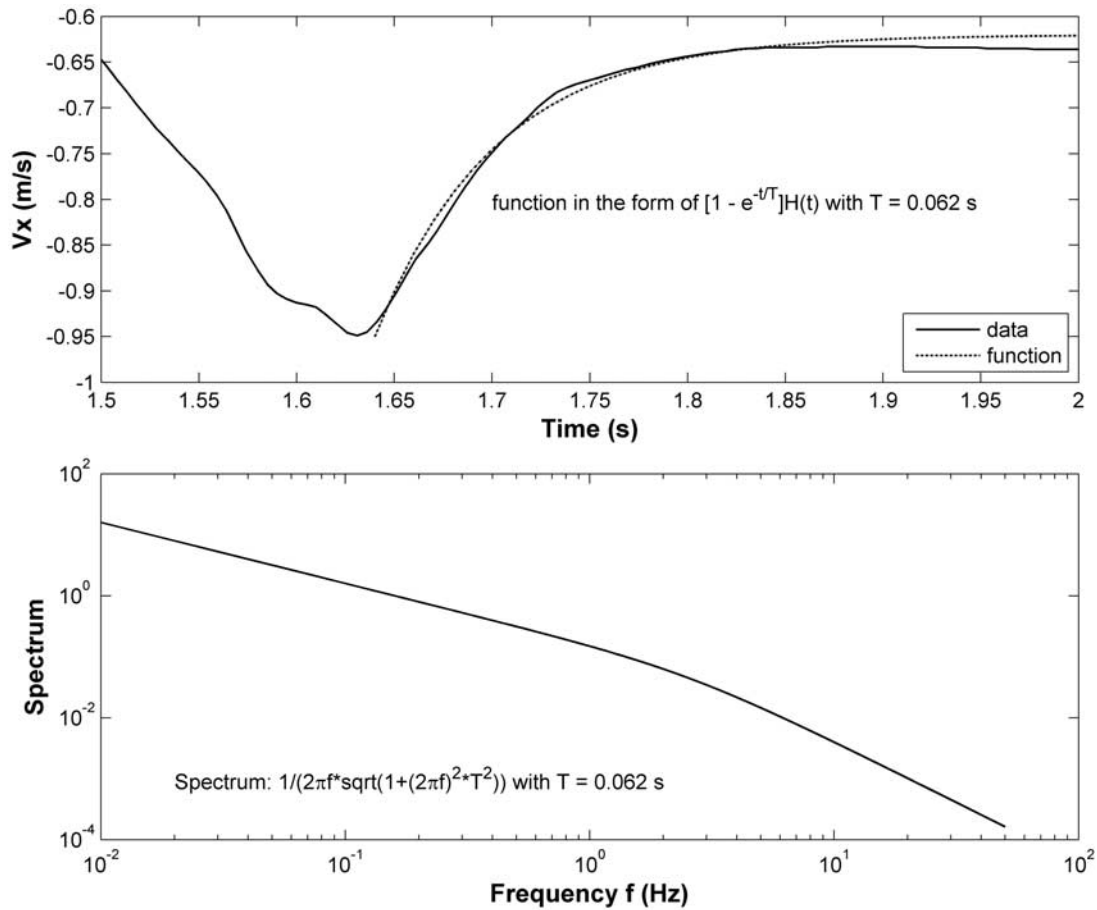
Figure 9. (a) Fit of seismic radiation from a kink by the function $[1 - \exp(-t/T)]H(t)$. (b) Spectrum of the fitting function and the ''corner'' frequency of reduction of high-frequency radiation.

elastic calculation after the arrival of the kink radiation (around 1.5 s), indicating more complex effects of off-fault plastic yielding on particle velocity at these stations. Figure 11 shows x-component particle velocities at stations in the S direction with different distances from the kink. Reduction of high-frequency radiation from the kink is observed at all these stations. Using the same procedure as in Figure 9, we can quantify the reduction. We found that
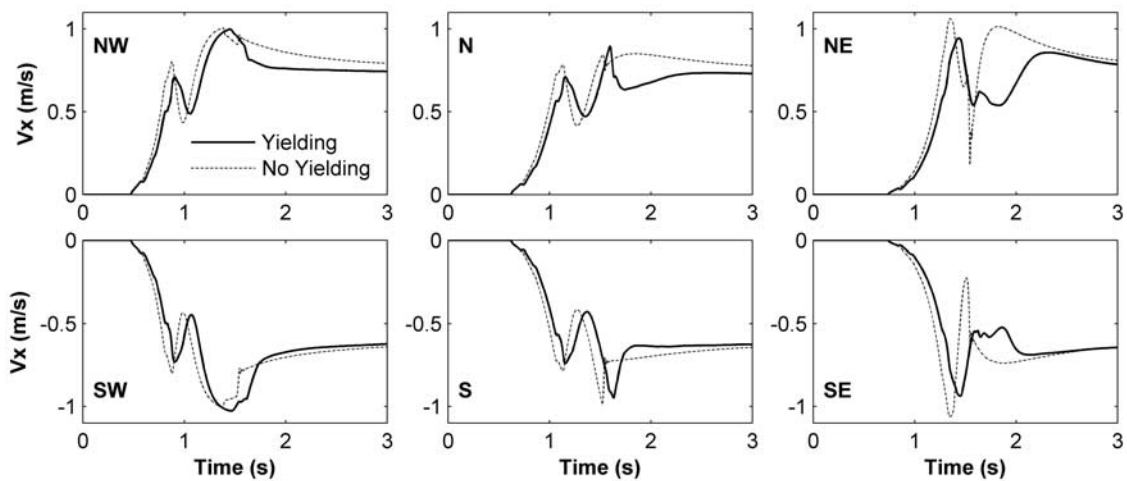

Figure 10. Particle velocity time histories at six stations shown in Figure 5. Reduction of high-frequency radiation from the fault kink by off-fault plastic yielding is obvious at stations S, SW, and NW but not obvious at Station N. Particle velocity due to the kink radiation is significantly different from elastic and elastoplastic calculations at stations NE and SE.
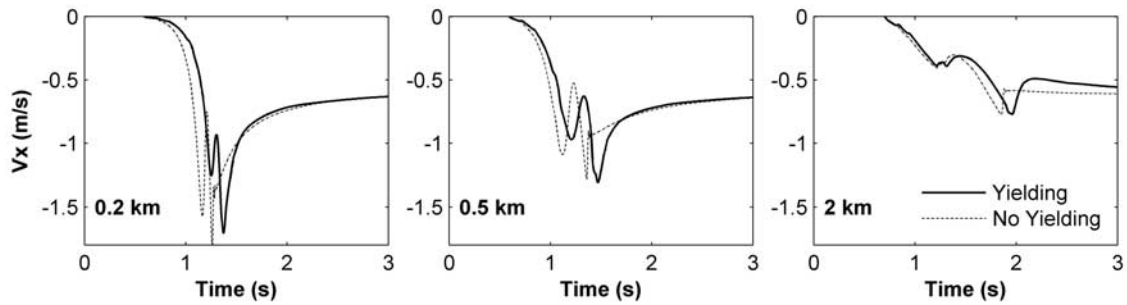
Figure 11. Particle velocity time histories at 3 stations with different distances from the kink in the S direction. Reduction of high-frequency radiation from the kink due to plastic yielding is observed at all stations without systematic variation in the "corner" frequency.

there is no systematic variation in the "corner" frequency with the distance away from the kink. Reduction of high-frequency radiation is significant above several Hz at these stations.

3.2. Variations in the Model

[36] To examine effects of model variations on the results, we perform several simulations with one of the following changes to the model in each simulation: (1) the length of incoming rupture to the kink; (2) the kink angle (change in fault strike); and (3) the sense of slip. Compared with the model in Figure 5, we set the hypocenter to be at (5500, 0) for (1) to allow a longer incoming rupture to the kink (4.5 km rather than 3 km), change the kink angle to be 5° for (2), and flip the sense of slip to be left-lateral for (3). Other model

parameters are same as the model (with $\Delta x = 5$ m) considered in section 3.1. We only discuss the results from elastoplastic calculations in this subsection.

[37] Figures 12 and 13 show the rupture time curves and the distributions of plastic strain magnitude from the three models, respectively. With a longer incoming rupture, the plastic strain zone associated with the kink and the right (post-bend) segment is wider (Figure 13a, compared with Figure 7). Plastic strain localization associated with the 5° kink is much weaker than that with the 10° kink. For example, the intensely-deformed band extending in the SEE direction is much shorter (Figure 13b). Even with off-fault plastic yielding, the 5° kink does not decrease rupture speed significantly (Figure 12, dashed curve). When the sense of slip becomes left-lateral, the right fault segment is more
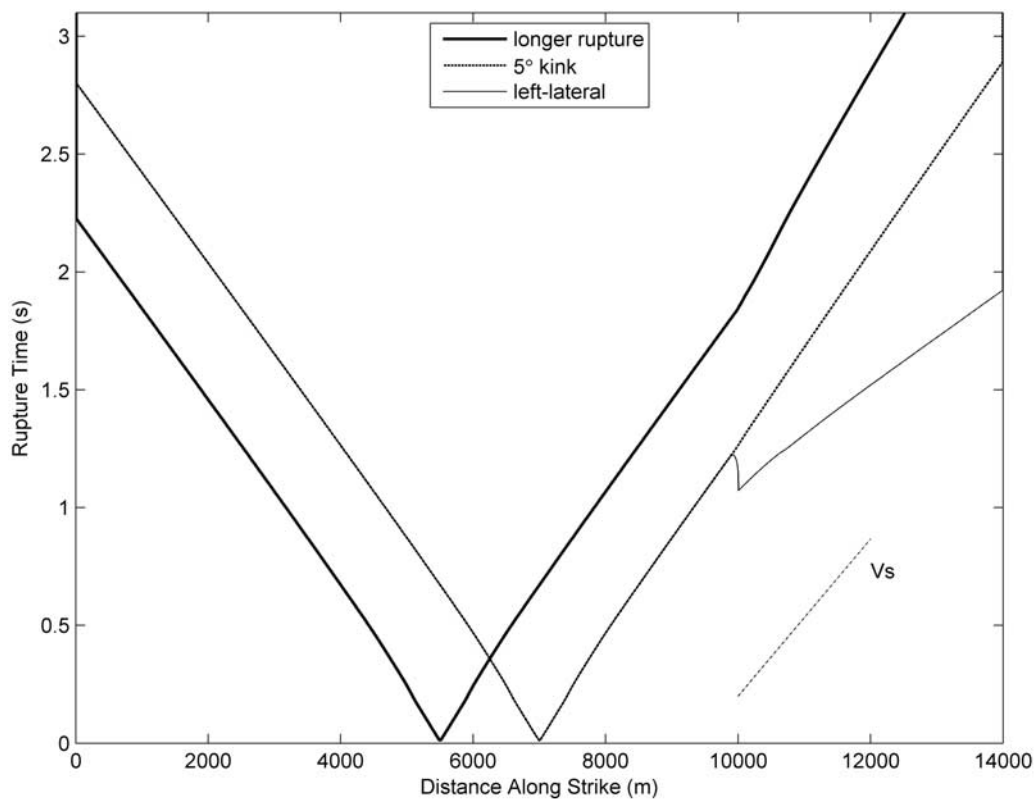

Figure 12. Rupture times from the models of a longer incoming rupture, a 5° kink angle, and a left-lateral fault with off-fault elastoplastic response.
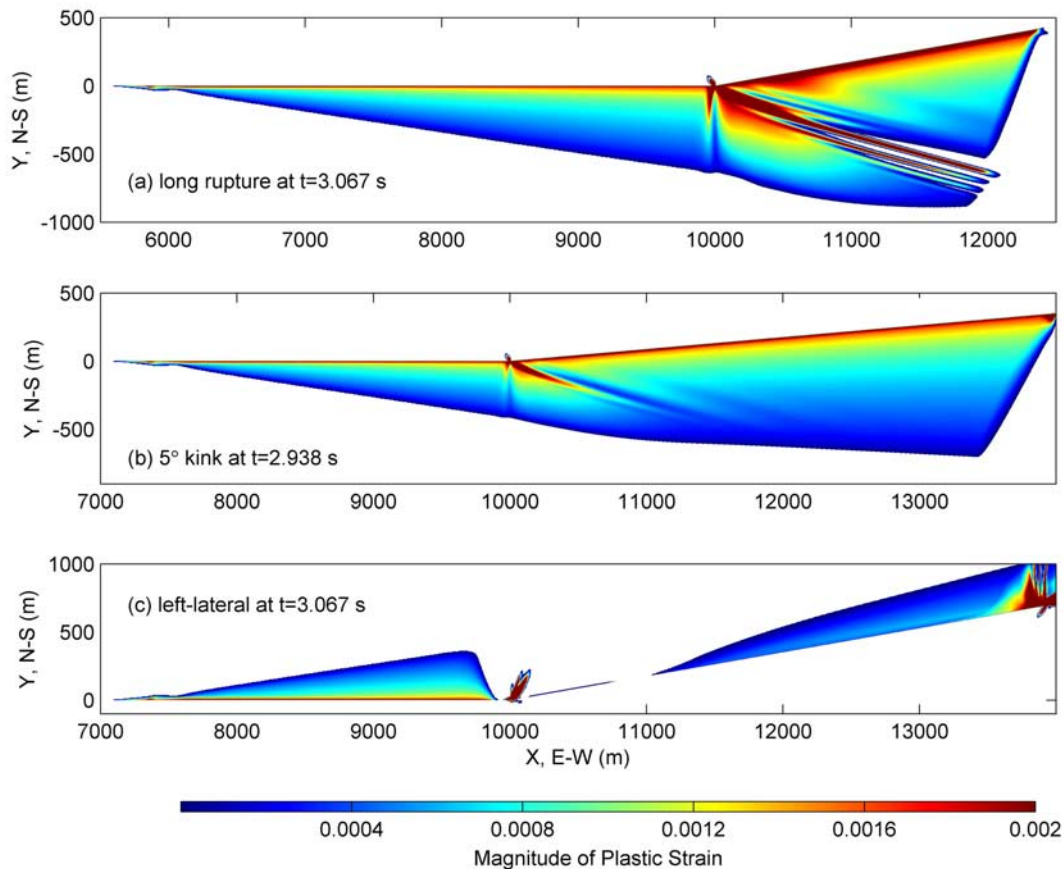
Figure 13. The distribution of plastic strain magnitude from the models of a longer incoming rupture, a 5° kink angle, and a left-lateral fault.

favorable for rupture in the uniform initial stress field than is the left segment. The rupture becomes supershear at the kink in both elastic (not shown) and elastoplastic (light solid curve in Figure 12) calculations. As shown in Figure 13c, the plastic strain occurs above the fault along this part of the fault in the model. Interestingly, except for a small plastic strain lobe, plastic strain is largely absent near the kink and to its right, and is even absent from a small patch just to the left of the kink. These gaps in plastic strain arise from a large extensional increment in the normal stress induced ahead of the rupture front on the right segment by left-lateral faulting on the left segment. Because of the resulting drop in frictional resistance to the right of the kink, the rupture jumps ahead to break the right segment before rupture reaches the kink from the left. The lowered frictional resistance permits the right segment to rupture at low shear-stress levels, permitting a supershear transition to occur and suppressing yielding over an extended region to the right of the kink. Meanwhile, slip immediately to the right of the kink puts the kink region (and the small patch just to its left) under compressive stress before the main rupture advancing from the left can arrive to put the kink region into extension. Thus the early-arriving compressive stresses from the right-segment crack tip suppress yielding that would otherwise be expected at the kink and just to its left.

[38] Particle velocity waveforms at Station S from the models of the longer incoming rupture and the 5° kink are compared with those from the model of the section 3.1 in Figure 14. At this station, the last velocity jump in the waveforms results from the kink radiation. As discussed before, the inverse rise time (initial slope of this jump divided by the amplitude of the jump) indicates the transition frequency for reduction of the high-frequency kink radiation by yielding. It can be seen that a longer incoming rupture results in a longer rise time (heavy curve versus light curve), suggesting a lower transition frequency that corresponds to a wider plastic strain zone near the kink (Figure 13a). This result qualitatively follows expectations from similarity for a rate-independent material model: when there is geometric similarity, all times should scale with the fundamental length dimension, a role that in this case, before fault end effects become significant, is played by the rupture distance to the kink. The foregoing applies for time histories at the same scaled distance, whereas the comparison in Figure 14 is for fixed unscaled distance, but we have already established that the kink-pulse rise time remains approximately invariant with propagation distance. The scaling of rise time is not exact, because we held fixed the friction parameter D_0 (had we scaled it with rupture distance to the kink, the scaling would have been exact, prior to the intervention of wave arrivals from the fault ends).
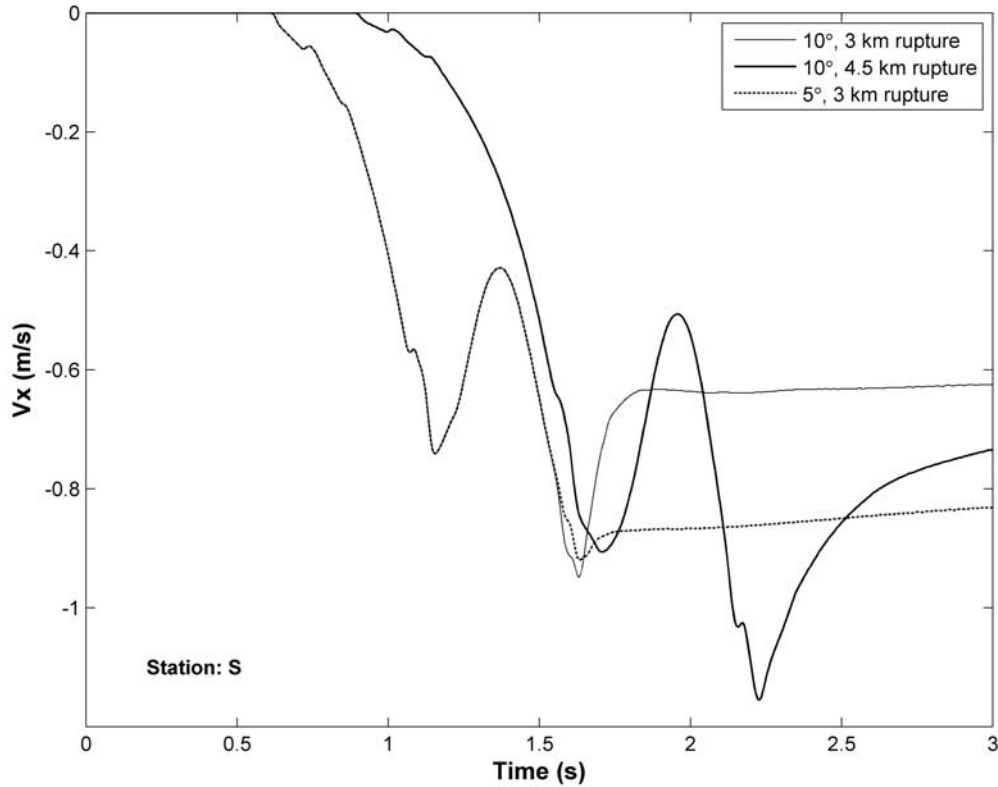
Figure 14. Particle velocity time histories at Station S from models of a longer incoming rupture and a 5° kink angle, compared with that from the model with 3 km incoming rupture and 10° kink angle. The inverse rise time of the last velocity jump in these curves indicates the transition frequency for reduction of high-frequency kink radiation by yielding.

[39] We also see in Figure 14 that (given the same incoming rupture length of 3 km) the 5° kink results in a slightly reduced kink-pulse rise time relative to the 10° kink, suggesting a slightly higher transition frequency, reflecting the less pronounced plastic strain localization seen in Figure 13b. Finally, as expected from the very minimal plastic strain near the kink in Figure 13c, particle velocities from the left-lateral model (not shown) do not exhibit any reduction in high-frequency radiation from the kink in the elastoplastic calculation with respect to the elastic calculation.

4. Localization of Off-Fault Plastic Strain in Planar Fault Models

[40] In the above section, we observe localization of off-fault plastic strain associated with a fault kink. In particular, strong plastic strain bands develop to accommodate a change in fault strike when rupture propagates onto a less favorable fault segment. The solution of plastic strain localization associated with a fault kink appears to be nearly (though not perfectly) grid independent, as demonstrated by solution comparisons with the element size reduced. This solution is achieved with viscoplastic regularization in which the relaxation time Tv (0.0017 s, see Table 2) is chosen as the time for an S wave to propagate one element ($\Delta x = 5$ m). When we reduce Tv, particularly with Tv = 0 s (without viscoplastic regularization), we find that plastic

strain localization can occur spontaneously even along a planar fault, under some initial stress conditions, while it does not occur under other conditions. In this section, we characterize the condition of plastic strain localization in planar fault models and discuss challenges in numerically simulating this phenomenon.

4.1. Determinant Factor: Relative Strength of Off-Fault Material

[41] On the basis of a large number of numerical experiments, we find that, for the class of model studied here (Mohr-Coulomb material, slip-weakening friction), pre-event proximity of the off-fault material to the failure level determines whether the coseismic inelastic strain will be smoothly distributed or will spontaneously localize into shear bands. We propose a parameter T to characterize how close the off-fault material is to the yield strength before an earthquake. Parameter T is defined as

$$T = \frac{\tau^0_{max}}{\tau^0_{coulomb}}, \qquad (14)$$

where τ^0_{max} and $\tau^0_{coulomb}$ are defined by equations (8b) and (11), respectively, with the initial values of the stress components used. T depends on the initial stress state and the material properties c (cohesion) and ϕ (the internal friction angle). The larger the T value is, the closer the initial state of the off-fault material is to failure.
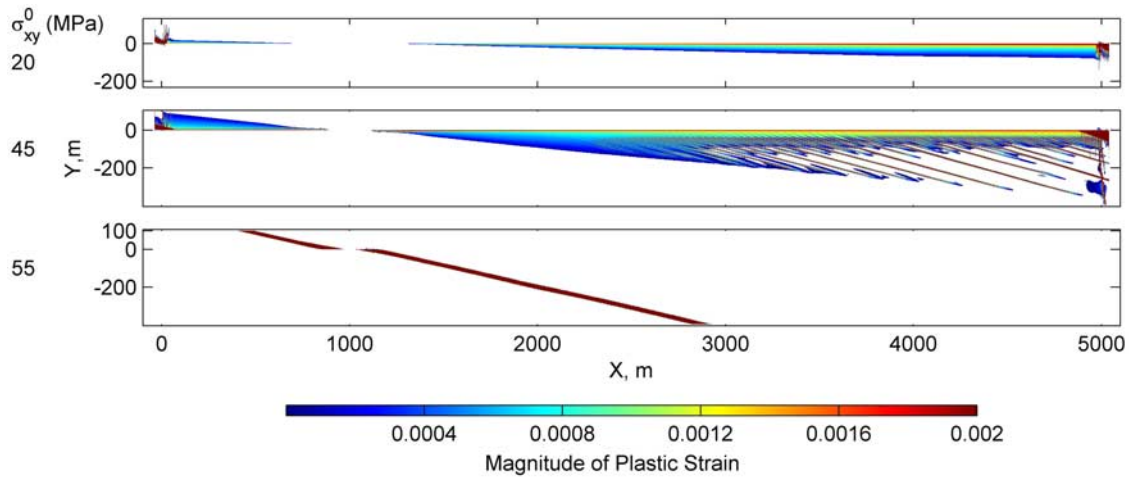
Figure 15. The distribution of plastic strain magnitude under three different initial shear stress conditions in a planar fault model. Higher initial shear stress promotes plastic strain localization.

[42] Figure 15 shows the plastic strain distribution at time 2.4 s from one set of numerical experiments on a 2D planar fault model (right-lateral, in-plane) with different initial shear stresses. The fault is 5 km long with two ends pinned by a high frictional coefficient. Rupture starts at $x = 1$ km, within a nucleation patch with a half length of 120 m. Material properties (velocity, density, cohesion, and internal friction) are same as those in Table 2. Numerical parameters $\Delta x = 2$ m, $\alpha = 0.4$, $\beta = 0.1$, and Tv = 0 s and the linear slip-weakening friction law with $D_0 = 0.04$ m are used in these simulations. The initial stress conditions and fault frictional coefficients in these calculations are listed in Table 3. We keep the seismic ratio S (1.5) and the static stress drop (10 MPa) same so that these simulations would give identical solutions for rupture propagation if off-fault response were purely elastic. The seismic ratio S defines how close a fault is to the failure level before an earthquake [e.g., *Andrews*, 1976; *Das and Aki*, 1977; *Day*, 1982]. In this set of simulations, a lower initial shear stress corresponds to a smaller T value as shown in Table 3. In the case of $\sigma_{xy}^0 = 20$ MPa (top) with $T = 0.33$, the distribution of plastic strain is smooth, similar to that in the model of *Andrews* [2005]: the magnitude of plastic strain is maximum adjacent to the fault and decreases continuously away from the fault. In the case of $\sigma_{xy}^0 = 45$ MPa (middle) with $T = 0.75$, plastic strain distribution is smooth within the first ~ 1.3 km rupture distance, then small-scale, poor-separated plastic strain bands appear within the next ~ 0.7 km rupture distance, and, finally, plastic strain localizes into discrete, well-separated bands away from the fault with poor-separated bands near the fault, and this pattern persists for the remaining ~ 2 km rupture distance to the right. The magnitude of plastic strain is larger in these well-separated bands than it is near the fault. Outside of these well-separated bands, plastic strain is absent. Nevertheless, in these two cases, rupture on the fault propagates continuously to the ends of the fault, with a faster rupture speed (not shown) in the case of $\sigma_{xy}^0 = 20$ MPa. Fault ends are associated with large plastic strain. In the case of $\sigma_{xy}^0 = 55$ MPa (bottom) with $T = 0.92$, rupture on the fault dies out

quickly outside the artificial initiation patch, while plastic deformation propagates along a favorable direction, resulting in two straight plastic strain bands emanating from the two ends of the fault rupture. In this case, the fault static friction coefficient ($\mu_s = 0.7$) is very close to that of off-fault material (0.75), and the fault plane is no longer the plane nearest failure under the given initial stress field. The above behavior show that larger values of T are associated with a higher degree of off-fault plastic strain localization into discrete shear bands.

4.2. Challenges in Numerically Modeling the Off-Fault Plastic Strain Localization

[43] The poorly-separated plastic strain bands in the above model with $\sigma_{xy}^0 = 45$ MPa impose a challenge to numerical resolution. Numerical experiments show that it is difficult to obtain a convergent solution for plastic strain localization in the planar fault model. Figure 16 shows the distribution of plastic strain magnitude for this model with another two element sizes, one smaller ($\Delta x = 1$ m) and one larger (4 m) than the 2 m used for the results shown in Figure 15. From Figure 16 together with Figure 15 (middle), it can be seen that the features of the plastic strain distribution continue to change as the element size is reduced. In the case of 4 m, the banding feature only appears at the right end of the model. The bands are not well-separated and the smooth feature dominates elsewhere. With decrease in the element size, the banding feature occurs progressively earlier and becomes dominant, while the zone with smooth plastic strain progressively shrinks. The transitions from the smooth feature, to the poor-separated bands, and further to

Table 3. Initial Stresses, Frictional Coefficients, and Parameter T for Simulation in Section 4.1

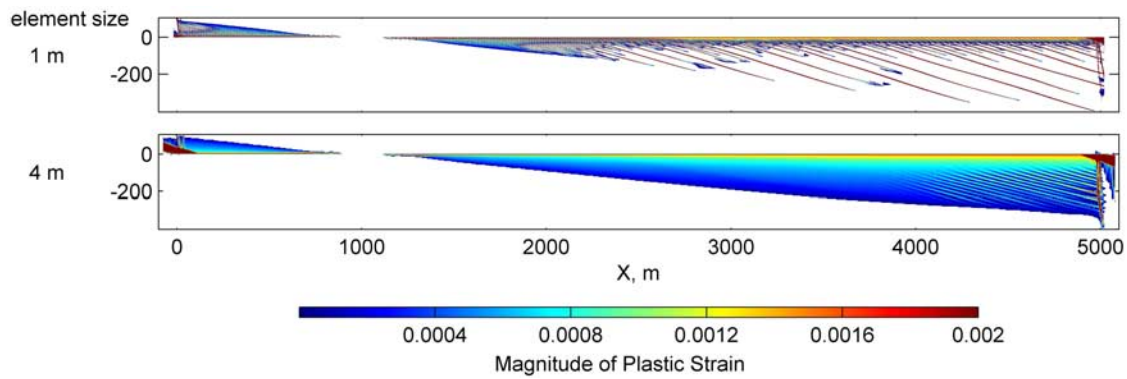| σ_{xx}^0 (MPa)	σ_{yy}^0 (MPa)	σ_{xy}^0 (MPa)	μ_s	μ_d	T
−100	−100	20	0.35	0.1	0.33
−100	−100	45	0.6	0.35	0.75
−100	−100	55	0.7	0.45	0.92

Figure 16. The distribution of plastic strain magnitude in a planar fault model with two different element sizes. Features of plastic strain localization keep changing with the element size, imposing a challenging in numerically simulating the localization.

the well-separated bands, are observed in both the 2 m and 1 m cases. However, for the well-separated bands, we do not see a trend toward strict convergence: the location and separation (e.g., perpendicular distance) between adjacent bands are different between the two cases. In these calculations, we adjust the dimensionless numerical parameter β (keeping the dimensional damping q fixed) to ensure that the same amount of damping is used with different element sizes.

[44] The time-dependent relaxation of stress adjustment (viscoplasticity) does not in general prevent plastic strain localization from occurring, though it delays the onset of plastic strain bands. Figure 17 shows the result on a longer fault (10 km) with Tv = 0.0006 s. Other parameters are the same as those in the above model with $\Delta x = 2$ m. Plastic strain localization occurs after rupture propagates more than 5 km and poor-separated bands have not been smoothed out by using this numerical regularization.

5. Discussion

5.1. Conditions and Significance of Off-Fault Plastic Strain Localization

[45] Previous theoretical studies on quasi-static deformation [e.g., *Rudnicki and Rice*, 1975; *Rice*, 1976] suggest that a pressure-dependent elastoplastic constitutive description, such as the Mohr-Coulomb yielding criterion, can be prone to localization of deformation. They introduced a critical hardening, h_{cr}, above which localization cannot occur. A

recent dynamic analysis [*Templeton and Rice*, 2008], using a similar constitutive description (the Drucker-Prager yield criteria), also shows features of dynamic plastic strain localization under some conditions. Whether or not plastic strain localization must occur when a material has a hardening value smaller than h_{cr} is not clear from these previous studies. With the stress condition and material properties in section 4.1, h_{cr} is positive, (whereas the models have a hardening value of 0). Given the grid resolutions we can achieve at present, plastic strain localization does not always occur in dynamic analyses even when the material hardening is smaller than h_{cr}. Rather, the parameter T proposed in the above section controls whether or not localization occurs, with a large value of T promoting localization. Under the condition of high T values on a planar fault model, the spontaneous-localization of plastic strain appears grid-dependent in its structural details, which may result from inherently scale-independent interactions among incipient shear bands that are cut off at the smallest scale accessible the numerical mesh. Exploration of numerical schemes that could prevent grid-dependent localization will be future work.

[46] Discrete, well-separated plastic strain bands in the models may represent well-developed secondary faulting, while smoothly distributed plastic strain may correspond to distributed fractures within a volume. In addition, our models also suggest that localization of off-fault plastic strain can strongly perturb rupture propagation on the main fault. In the end-member case in which the static strength of
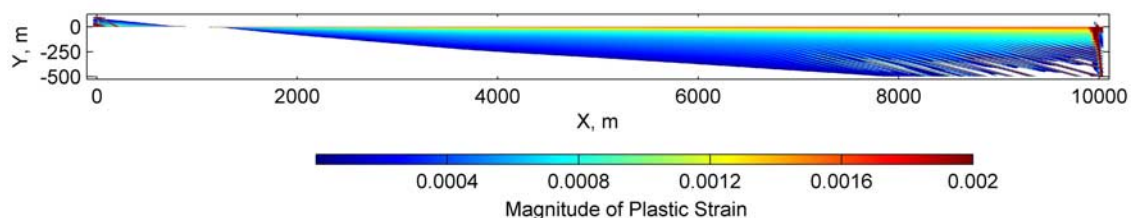

Figure 17. The distribution of plastic strain magnitude in a longer planar fault model with viscoplasticity regularization. This regularization can only delay onset of plastic strain bands without removing small-scale, poor-separated features.
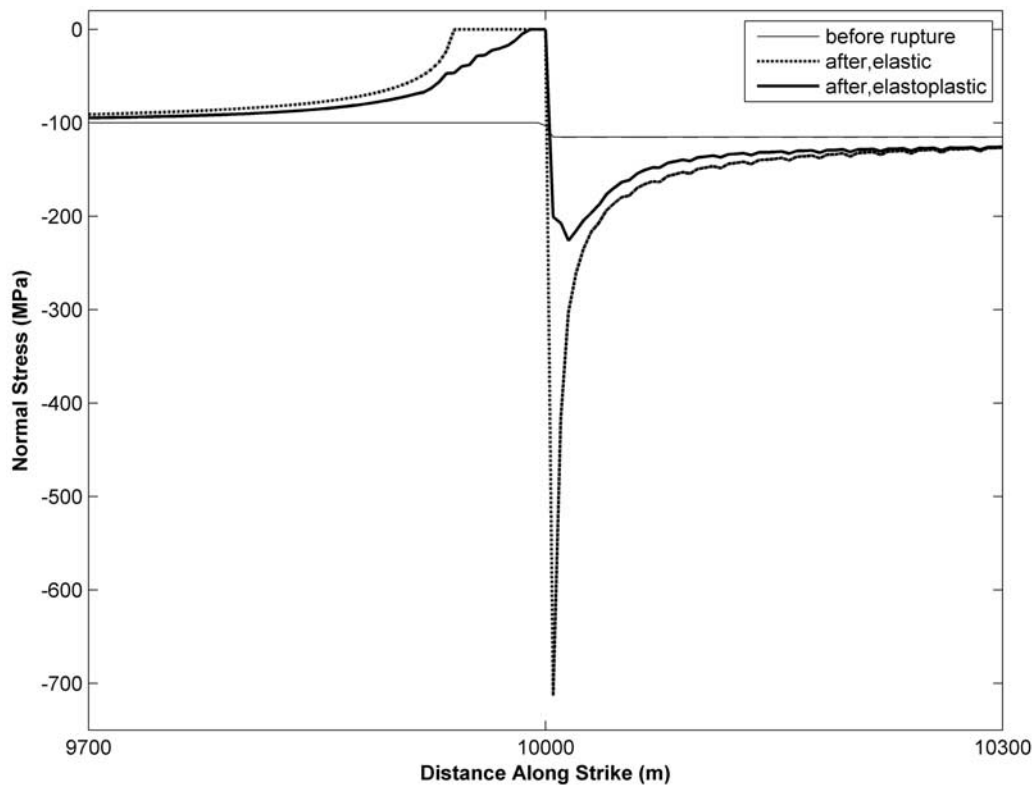
Figure 18. Fault normal stress near a kink before and after a seismic rupture. Off-fault plastic yielding significantly reduces magnitude of the stress to the right of the kink and width of fault opening zone to the left of the kink.

the fault is close to the strength of the surrounding material, for example, off-fault strain bands develop while rupture on the pre-existing fault dies out (e.g., in the model of $\sigma^0_{xy} = 55$ MPa in section 4.1). Thus different damage distributions in the field may give us some clues about relative strength between a main fault and the surrounding host rocks: if there is significant secondary faulting, it may indicate the strength of the main fault is close to that of the host rocks; more diffuse damage may be characteristic when the strength of the main fault is significantly lower than that of the host rocks.

5.2. Effects of Off-Fault Plastic Yielding on Residual Stresses at a Fault Kink

[47] In examining long-term effects of non-planar fault geometry on repeated seismic ruptures, *Nielsen and Knopoff* [1998] and *Duan and Oglesby* [2005] introduced a viscoelastic model to avoid pathological stresses at fault kinks that would be accumulated over repeated ruptures. This viscoelastic model may represent aseismic stress relaxation at fault kinks. However, nonelastic deformation near a fault kink during dynamic ruptures is absent in these previous studies. Although aseismic stress relaxation may occur during the inter-seismic period and play an important role in limiting stress buildup at fault irregularities, we expect that off-fault nonelastic deformation during dynamic ruptures can also have large effects on accumulated stresses at these locations. Figure 18 shows the fault-normal stress near the fault kink before and after the seismic rupture from calcu-

lations in section 3.1, comparing results with off-fault elastic and elastoplastic response, respectively. The normal stress before the seismic event is same for the two calculations. After the seismic rupture, the normal stress from the two calculations is different near the kink. The very large compressive normal stress to the right side of the kink in the elastic calculation is significantly reduced (to about one third) because of yielding in the elastoplastic calculation. In these calculations, we allow the fault to open when the fault normal stress becomes tensile, and fault opening results in zero fault-normal stress. This occurs to the left side of the kink in both calculations. However, plastic flow significantly reduces the width of this fault opening zone. Thus coseismic nonelastic deformation near fault irregularities has large effects on residual stresses at these locations and needs to be accounted for in more realistic multiple earthquake cycle models.

5.3. Contribution of Off-Fault Plastic Yielding to Cohesive Zone Development and Equivalence Between Time-Weakening and Slip-Weakening Friction Laws

[48] Resolving the cohesive zone at the rupture front is crucial for capturing peak slip rates and rupture propagation speeds. The cohesive zone is the portion of the fault plane behind the rupture front where the frictional coefficient decreases from its static value to its dynamic value and slip s satisfies $0 < s < D_0$ [e.g., *Andrews*, 1976; *Day et al.*, 2005]. In elastodynamic analyses (where off-fault response is
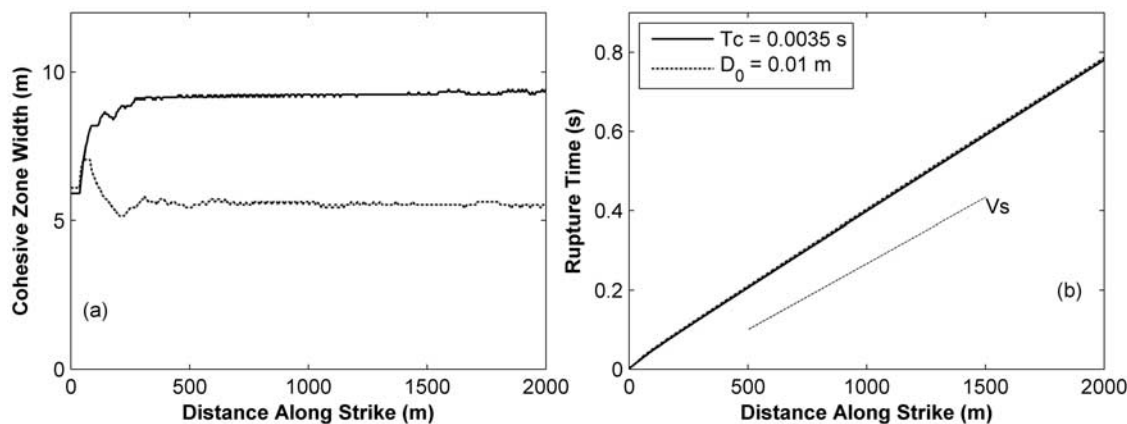
Figure 19. (a) Cohesive zone width and (b) rupture time along a planar fault from two calculations with off-fault plastic yielding: one uses a time-weakening friction law, the other uses a slip-weakening friction law. The legend in Figure 19b also applies to Figure 19a.

assumed to be purely elastic), a linear slip-weakening friction law with a constant critical slip distance D_0 results in shrinking of the cohesive zone width with increasing rupture velocity v_r, the width approaching zero as terminal velocity (the Rayleigh velocity in the plane strain case) is approached. Rupture velocity in turn grows with rupture propagation distance (assuming conditions of uniform stress drop and 2D geometry), so the cohesive-zone width contracts with propagation distance in the elastodynamic case. A linear time-weakening friction law can avoid this narrowing of the cohesive zone with propagation distance, and results in an effective D_0 that is proportional to the square root of rupture propagation distance [*Andrews*, 2004; *Day et al.*, 2005].

[49] With off-fault plastic yielding, however, the cohesive zone development may be quite different than in the elastodynamic case. *Day et al.* [2005] speculated that plastic yielding might thereby re-set the minimum scale for numerical resolution, and we explore that idea here. Figure 19 compares cohesive zone development and rupture propagation between two calculations on the model by *Andrews* [2005] (see section 2.4). One calculation uses the time-weakening friction law with Tc = 0.0035 s. The other calculation uses the linear slip-weakening law with D_0 of 0.01 m. Other parameters, such as Tv of 0.00067 s and the element size of 2 m, are same between the two calculations. It can be seen from Figure 19a that the cohesive zone width in the slip-weakening model does not shrink appreciably with rupture propagation distance when there is interaction with off-fault plastic yielding. Rather, it tends to become a constant. The cohesive zone width in the case of the time-weakening law with Tc = 0.0035 s also stabilizes quickly outside of the nucleation patch. From Figure 19b, one can see clearly that the slip-weakening model with $D_0 = 0.01$ m gives almost the same solution for rupture propagation on the fault as the time-weakening model. Thus these two friction laws become essentially equivalent when off-fault plastic yielding is included in the models.

[50] This equivalency arises because off-fault yielding limits the rupture velocity, stopping the scale contraction at the rupture front (Figure 19b shows that rupture velocity

quickly stabilizes at a value below terminal velocity). We can also understand the stabilization of the cohesive scale more directly by the following argument. When there is a strength limit in the material adjacent to the fault, the very high slip velocities present at the rupture front in elastodynamic models are suppressed, and a nearly constant slip rate develops as yielding occurs at and just behind the rupture front. The constant slip rate results in a nearly constant effective D_0 as a function of rupture propagation distance in the time-weakening model (and a constant effective T_c in the slip-weakening model). Put differently, if (in the slip-weakening context) most of the critical slip D_0 occurs while slip velocity is capped at some value $\dot{s}_{max}$ because of yielding, then a new minimum cohesive scale length of order $D_0 V_r / \dot{s}_{max}$ is introduced, and this scale puts a limit on cohesive-zone contraction.

[51] Numerical resolution of the cohesive width by several grid elements is essential to solution accuracy of rupture propagation problems. In the case of $D_0 = 0.01$ m, the cohesive zone width is about 6 m (3 elements). Although it is narrower than that from Tc = 0.0035 s (about 9 m, 4.5 elements), the good agreement between these two calculations seen in Figure 19b suggests that both models well resolve the cohesive zone and the solution has a good accuracy. This inference is also consistent with the finding in the study by *Day et al.* [2005], using a similar numerical method, that 3-element resolution of the cohesive zone was adequate to capture rupture propagation speed to an accuracy of about 1%. In comparison, if yielding were suppressed, the same element size of 2 m would require a D_0 value of about 0.06 m to well resolve the cohesive zone (i.e., 3 elements within the zone) at a rupture distance of 2 km based on an elastodynamic analysis [*Andrews*, 2004].

6. Conclusions

[52] Numerical simulations for a Mohr-Coulomb material predict substantial inelastic deformation in association with rupture along both straight and kinked faults. In the straight-fault case, deformation may be smoothly distributed or may spontaneously localize into discrete shear bands, depending

upon the initial stress state and the material strength parameters (i.e., cohesion and internal friction). For uniform initial stress, the determinative parameter controlling spontaneous localization is the ratio $\tau_{max}/\tau_{coulomb}$ (defined by equations (8b) and (11)). If these distinct damage modes (smoothly distributed versus localized) arising in idealized models have approximate counterparts in real faulting, then field patterns of damage and secondary faulting may provide information about relative strength between fault surface and host rock, with, e.g., a more localized damage mode being inductive of bulk and frictional strength that are relatively close in value.

[53] In the case of a kinked-fault, extensive inelastic deformation concentrates near a restraining bend, principally on the side of the fault associated with rupture-front extensional strains, the deformation taking the form of a few distinct lobes and shear bands. The spatial extent and intensity of the deformation both increase with increasing restraining-bend angle, and become relatively much smaller in the case of a releasing-bend orientation. For some azimuths, the inelastic strain reduces the high-frequency seismic radiation originating from the kink, with the far-field spectrum of this phase diminishing by an extra factor of f^{-1} (relative to the corresponding perfectly elastic model), above a frequency of several Hz. The coseismic inelastic strain also greatly reduces the residual stress concentrations left behind after rupture through a fault bend (e.g., residual normal stress reduction of a factor of 3 in a typical $10°$ restraining bend case), with potentially significant consequences for models of fault-system evolution through multiple-earthquake cycles.

[54] Rupture simulations for the Mohr-Coulomb material model raise some computational issues not present in corresponding perfectly elastic problems. Our comparison with published results by *Andrews* [2005] suggests that numerical solutions for those rupture models with smooth strain distributions can be reproduced to high precision when done with different numerical methods and different (but sufficiently refined) grids. When localized shear bands are induced at an isolated, discrete concentrator like a fault kink, the essential features of the solution appear to be grid independent, but some grid dependence persists in the details of the final strain distribution. Finally, in the case where multiple shear bands develop spontaneously, the bands appear to interact strongly at the smallest spatial scales accessible to the grid, and we therefore do not obtain strict numerical convergence as the grid is refined. On the other hand, plastic yielding suppresses the scale contraction of the fault cohesive zone that otherwise occurs in perfectly elastic rupture propagation models, thereby improving the prospects for numerical resolution of the short-scale lengths induced by frictional breakdown.

References

Adda-Bedia, M., and R. Madariaga (2008), Seismic radiation from a kink on an antiplane fault, *Bull. Seismol. Soc. Am.*, *98*, 2291–2302, doi:10.1785/0120080003.

Andrews, D. J. (1976), Rupture velocity of plane strain shear cracks, *J. Geophys. Res.*, *81*(32), 5679–5687.

Andrews, D. J. (1999), Test of two methods for faulting in finite-difference calculations, *Bull. Seismol. Soc. Am.*, *89*(4), 931–937.

Andrews, D. J. (2004), Rupture models with dynamically-determined breakdown displacement, *Bull. Seismol. Soc. Am.*, *94*, 769–775.

Andrews, D. J. (2005), Rupture dynamics with energy loss outside the slip zone, *J. Geophys. Res.*, *110*, B01307, doi:10.1029/2004JB003191.

Andrews, D. J., T. C. Hanks, and J. W. Whitney (2007), Physical limits on ground motion at Yucca Mountain, *Bull. Seismol. Soc. Am.*, *97*, 1771–1792, doi:10.1785/0120070014.

Aochi, H., E. Fukuyama, and M. Matsu'ura (2000), Spontaneous rupture propagation on a non-planar fault in 3-D elastic medium, *Pure Appl. Geophys.*, *157*, 2003–2037.

Ben-Zion, Y., and C. G. Sammis (2003), Characterization of fault zones, *Pure Appl. Geophys.*, *160*, 677–715.

Ben-Zion, Y., Z. Peng, D. Okaya, L. Seeber, L. G. Armbruster, N. Ozer, A. J. Michael, S. Baris, and M. Aktar (2003), A shallow fault zone structure illuminated by trapped waves in the Karadere-Duzce branch of the North Anatolian fault, western Turkey, *Geophys. J. Int.*, *152*, 699–717, doi:10.1046/j.1365-246X.2003.01870.x.

Bouchon, M., and D. Streiff (1997), Propagation of a shear crack on a nonplanar fault: A method of calculation, *Bull. Seismol. Soc. Am.*, *87*, 61–66.

Chester, F. M., and J. S. Chester (1998), Unltrcataclasite structure and friction processes of the Punchbowl, San Andreas system, California, *Tectonophysics*, *295*, 199–221.

Chester, F. M., J. S. Chester, D. L. Kirschner, S. E. Schulz, and J. P. Evans (2004), Structure of large-displacement strike-slip fault zones in the brittle continental crust, in *Rheology and Deformation in the Lithosphere at Continental Margins*, MARGINS Theor. and Exp. Earth Sci. Ser., vol. 1, edited by G. D. Karner et al., pp. 223–260, Columbia Univ. Press, New York.

Dalguer, L. A., and S. M. Day (2007), Staggered-grid split-node method for spontaneous rupture simulation, *J. Geophys. Res.*, *112*, B02302, doi:10.1029/2006JB004467.

Das, S., and K. Aki (1977), A numerical study of two-dimensional spontaneous rupture propagation, *Geophys. J. R. Astron. Soc.*, *50*, 643–668.

Davis, R. O., and A. P. S. Selvadurai (2002), *Plasticity and Geomechanics*, Cambridge Univ. Press, Cambridge, New York.

Day, S. M. (1982), Three-dimensional simulation of spontaneous rupture: The effect of nonuniform prestress, *Bull. Seismol. Soc. Am.*, *72*, 1881–1902.

Day, S. M., L. A. Dalguer, N. Lapusta, and Y. Liu (2005), Comparison of finite difference and boundary integral solutions to three-dimensional spontaneous rupture, *J. Geophys. Res.*, *110*, B12307, doi:10.1029/2005JB003813.

Duan, B., and D. D. Oglesby (2005), Multicycle dynamics of nonplanar strike-slip faults, *J. Geophys. Res.*, *110*, B03304, doi:10.1029/2004JB003298.

Duan, B., and D. D. Oglesby (2006), Heterogeneous fault stresses from previous earthquakes and the effect on dynamics of parallel strike-slip faults, *J. Geophys. Res.*, *111*, B05309, doi:10.1029/2005JB004138.

Duan, B., and D. D. Oglesby (2007), Nonuniform prestress from prior earthquakes and the effect on dynamics of branched fault systems, *J. Geophys. Res.*, *112*, B05308, doi:10.1029/2006JB004443.

Ellsworth, W. L., and P. Malin (2006), A first observation of fault guided PSV-waves at SAFOD and its implications for fault characteristics, *Eos Trans. AGU*, *87*(52), Fall Meet. Suppl., Abstract T23E-02.

Ely, G., S. M. Day, and J.-B. Minster (2008), A support-operator method for 3D rupture dynamics, *Geophys. J. Int.*, in review.

Hughes, T. J. R. (2000), *The Finite Element Method: Linear Static and Dynamic Finite Element Analysis*, Dover, Nineola, New York.

King, G., and J. Nabelek (1985), Role of fault bends in the initiation and termination of earthquake rupture, *Science*, *228*, 984–987.

Li, Y. G., K. Aki, D. Adams, A. Hasemi, and W. H. K. Lee (1994), Seismic guided waves trapped in the fault zone of the Landers, California, earthquake of 1992, *J. Geophys. Res.*, *99*, 11,705–11,722.

Madariaga, R. (1977), High frequency radiation from crack (stress drop) models of earthquake faulting, *Geophys. J. R. Astron. Soc.*, *51*, 625–651.

Nielsen, S. B., and L. Knopoff (1998), The equivalent strength of geometrical barriers to earthquakes, *J. Geophys. Res.*, *103*(B5), 9953–9965.

Poliakov, A. N. B., R. Dmowska, and J. R. Rice (2002), Dynamic shear rupture interactions with fault bends and off-axis secondary faulting, *J. Geophys. Res.*, *107*(B11), 2295, doi:10.1029/2001JB000572.

Rice, J. R. (1976), The localization of plastic deformation, in *Theoretical and Applied Mechanics*, Proceedings of the 14th International Congress on Theoretical and Applied Mechanics, Delft, 1976, vol. 1, edited by W. T. Koiter, pp. 207–220, North-Holland, New York.

Rice, J. R., C. G. Sammis, and R. Parsons (2005), Off-fault secondary failure induced by a dynamic slip pulse, *Bull. Seismol. Soc. Am.*, *95*(1), 109–134, doi:10.1785/0120030166.

Rudnicki, J. W., and J. R. Rice (1975), Conditions for the localization of deformation in pressure-sensitive dilatant materials, *J. Mech. Phys. Solids*, *23*, 371–394.

Scholz, C. H. (2002), *The Mechanics of Earthquakes and Faulting*, 2nd ed., Cambridge Univ. Press, New York.

Tada, T., and T. Yamashita (1997), Non-hypersingular boundary integral equations for two-dimensional non-planar crack analysis, *Geophys. J. Int.*, *130*, 269–282.

Templeton, E. L., and J. R. Rice (2008), Off-fault plasticity and earthquake rupture dynamics. 1: Dry materials or neglect of fluid pressure changes, *J. Geophys. Res.*, *113*, B09306, doi:10.1029/2007JB005529.

_____

S. M. Day, Department of Geological Sciences, San Diego State University, 5500 Campanile Dr., San Diego, CA 92182, USA.

B. Duan, Department of Geology and Geophysics, Texas A&M University, 3115 TAMU, College Station, TX 77843-3115, USA. (bduan@tamu.edu)